

Article

Optical, Electrochemical and Hydrophilic Properties of YO Doped TiO Nanocomposite Films

Xiangchao Zhang, Huaming Yang, and Aidong Tang

J. Phys. Chem. B, **2008**, 112 (51), 16271-16279 • DOI: 10.1021/jp806820p • Publication Date (Web): 21 November 2008

Downloaded from <http://pubs.acs.org> on December 20, 2008

More About This Article

Additional resources and features associated with this article are available within the HTML version:

- Supporting Information
- Access to high resolution figures
- Links to articles and content related to this article
- Copyright permission to reproduce figures and/or text from this article

[View the Full Text HTML](#)



ACS Publications
High quality. High impact.

The Journal of Physical Chemistry B is published by the American Chemical Society, 1155 Sixteenth Street N.W., Washington, DC 20036

Optical, Electrochemical and Hydrophilic Properties of Y₂O₃ Doped TiO₂ Nanocomposite Films

Xiangchao Zhang,[†] Huaming Yang,^{*,†} and Aidong Tang[‡]

Department of Inorganic Materials, School of Resources Processing and Bioengineering, Central South University, Changsha 410083, China, and School of Chemistry and Chemical Engineering, Central South University, Changsha 410083, China

Received: April 23, 2008; Revised Manuscript Received: October 16, 2008

The 5% Y₂O₃ doped TiO₂ nanocomposite film (YTF) deposited on ITO glass substrate has been synthesized by the sol–gel dip-coating method. The as-synthesized samples were characterized using X-ray diffraction (XRD), atomic force microscopy (AFM), scanning electron microscope (SEM), X-ray photoelectron spectroscopy (XPS), voltage–current (*V–I*), electrochemical impedance spectroscopy (EIS) and ultraviolet–visible (UV–vis) analysis technologies. The crystalline structure, surface morphology and surface chemical composition of YTF sample have been primarily investigated. The results demonstrate that YTF is anatase crystalline phase with thickness of 480 nm and consists of spherical shape particles with a grain size of about 15.8 nm. The binding energy appears as a chemical shift, and relatively more Y and Ti species are present on the surface, indicating that active surfaces of the nanocomposite film have been enhanced with more oxygen vacancies V_O[•] due to doping Y₂O₃ to TiO₂. The absorption edge of YTF has a red shift, and the optical properties of YTF in visible light region have been obviously improved. The water contact angle is about 8° after daylight lamp irradiation 60 min. An equivalent circuit model provided a reliable description for the electrochemical systems. Based on the Mott–Schottky equation, the donor concentration (*N_D*) for YTF is $1.05 \times 10^{20} \text{ cm}^{-3}$, which enhances 1 order of magnitude than that for pure TiO₂ film (TF), the flat-band potential (*V_{fb}*) and the space charge layer (*d_{sc}*) obviously decreased. With the incorporation of Y₂O₃ into TiO₂, the optical, electrochemical and photoinduced hydrophilic properties of YTF in visible light region have obviously improved, indicating that YTF shows promising applications in solar energy conversion, self-cleaning and other potential fields.

Introduction

Since Fujishima discovered the photocatalytic splitting of water on a TiO₂ electrode under ultraviolet light,¹ enormous efforts have been devoted to the research of TiO₂ material due to its excellent optical, electrical, photocatalytic and thermal properties, which has led to many promising applications in areas ranging from photovoltaics and photocatalysis to sensors and potential tool in cancer treatment.^{2–7}

It is well-known that the electronic property of a material is closely related to its chemical composition (chemical nature of the bonds between the atoms or ions), atomic arrangement and physical dimension. The chemical composition of TiO₂ can be altered by doping. Specifically, Ti⁴⁺ or O^{2–} can be replaced to enhance the material's physicochemical properties. It is desirable to maintain the integrity of the crystal structure for the host material (TiO₂) and to produce favorable changes in electronic structure. Continuous efforts have been made to improve the properties of TiO₂ thin film, such as noble metal loading, metal ion doping, anion doping, dye sensitization, composite semiconductors and metal ion-implantation.^{8–12}

The preparation and application of TiO₂-based composite films are currently attracting attention; for example, Pan has successfully prepared the highly ordered cubic mesoporous WO₃/TiO₂ thin films, and their photocatalytic activities in

decomposing 2-propanol were 6.1 times than that of a nonporous TiO₂ film derived from a typical sol–gel method.¹¹ Vinodgopal reported that the degradation rate of a textile azo dye naphthol blue black (NBB) was significantly higher for SnO₂–TiO₂ composite films than SnO₂ or TiO₂ films.¹³ Tacconi also reported that Ni–TiO₂ composite films exhibited unusual photocurrent and played a concerted and complementary role in promoting the initial adsorption and subsequent photo-oxidation of sulfite.¹⁴ Poznyak investigated the structure, optical and photoelectrochemical properties of TiO₂–In₂O₃ composites with different molar ratio of TiO₂ to In₂O₃.¹⁵ According to Kwon's research, the photocatalytic decomposition of TiO₂–SiO₂ nanocomposite thin films for methylene blue increased and the contact angle decreased with increasing the percentage of TiO₂ phase.¹⁶ Bartl treated Cd²⁺-doped TiO₂ films with sulfur or selenium vapor; the as-synthesized mesoporous CdS/TiO₂ or CdSe/TiO₂ thin films showed an enhanced sensitivity to visible light.¹⁷ Liang found that the optical properties of the ZrO₂–TiO₂ composite films could be easily tailored in a wide range via a simple control on the system composition.¹⁸ Barreca synthesized ZnO–TiO₂ nanocomposites and investigated the gas-sensing performances in the detection of volatile organic compounds (CH₃COCH₃, CH₃CH₂OH and CO); the ZnO–TiO₂ nanocomposites showed intriguing perspectives for the development of sensing devices for environmental purposes and food control monitoring.¹⁹ Chen studied the photoelectron–chemical performance and photocatalytic activities of ZnO–TiO₂ nanocomposites; the generated photocurrent was largely enhanced with several orders of

* Corresponding author. Tel: +86-731-8830 549. Fax: +86-731-8710 804. E-mail address: hmyang9392@hotmail.com.

[†] School of Resources Processing and Bioengineering.

[‡] School of Chemistry and Chemical Engineering.

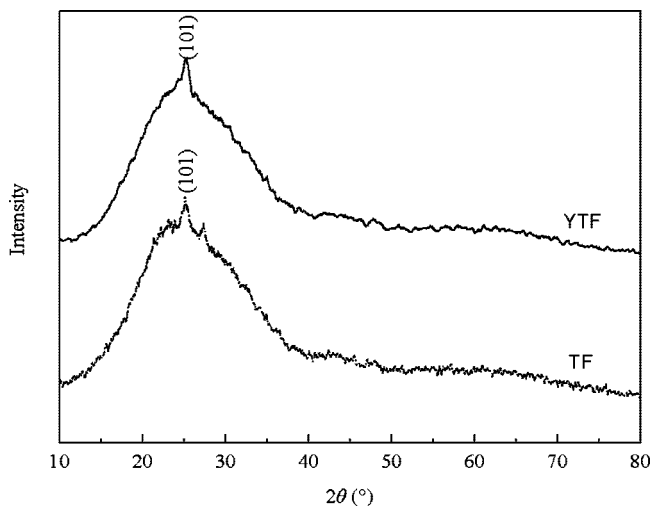


Figure 1. XRD patterns for TF and YTF deposited on ITO substrate.

magnitude higher intensities than that of the TiO_2 nanoparticles or ZnO nanorods.²⁰ As we know, the properties of composites often cannot be considered as a simple superposition of the properties of individual component due to strong surface interactions between the closely packed nanoparticles in the binary oxide systems.²¹ The photocurrent actions and photocatalytic activities might arise from enhancing the light harvest and the ability of generating photoinduced electron–hole pairs of active sites, and the favorable electron-transfer properties of the heterojunctions in the nanocomposites.

However, to our knowledge, Y_2O_3 doped TiO_2 nanocomposite films have not been investigated. Yttrium oxide (Y_2O_3) is an important component in a wide variety of materials, including yttria-stabilized zirconia (YSZ), yttrium–aluminum or yttrium indium garnet (YAG or YIG), the perovskite phase YTiO_3 and especially the yttrium-based high conducting temperature superconducting metal oxides.²² In addition, Y_2O_3 could be used as a waveguide material due to its high refractive index, or as a buffer layer for ferroelectrics and superconductors because of its low lattice-mismatch with silicon. Y_2O_3 has also been investigated for use as optical and protective coating layers due to a high melting point and refractive index.²³ On the other hand, as red phosphor and display material, Y_2O_3 has attracted great interest about luminescence properties for the past few years.²⁴

In this work, the 5% Y_2O_3 doped TiO_2 nanocomposite films (YTF) deposited on ITO glass substrate have been synthesized by the sol–gel dip-coating method, the synthesis process and conditions used in the preparation of the precursor solution and films are evaluated by X-ray diffraction (XRD), atomic force microscopy (AFM), scanning electron microscope (SEM), X-ray photoelectron spectroscopy (XPS), voltage–current (V – I), electrochemical impedance spectroscopy (EIS) and ultraviolet–visible (UV–vis) absorption spectra. The optical, electrochemical and photoinduced hydrophilic properties of YTF are systematically analyzed and compared with the pure TiO_2 film (TF). It is expected that the present work is of notable significance for understanding the unique properties that result from the coupled nanocomposites and for designing new nanocomposites of advanced functions in photoelectrochemical, self-cleaning and antifogging applications.

Experimental Section

Preparation of Precursor Solutions. The precursor solution of Y_2O_3 doped TiO_2 sol was synthesized by a sol–gel method,

using titanium tetrabutoxide ($\text{Ti}(\text{OC}_4\text{H}_9)_4$, TTBO), diethanolamine ($\text{NH}(\text{CH}_2\text{CH}_2\text{OH})_2$, DEA), anhydrous alcohol ($\text{C}_2\text{H}_5\text{OH}$, EtOH) and yttrium nitrate ($\text{Y}(\text{NO}_3)_3 \cdot 6\text{H}_2\text{O}$, Y) as starting materials. All reagents were analytical grade and used without further purification. In typical synthesis process, 17.02 mL of TTBO and 4.8 mL of DEA were mixed with 48.28 mL of EtOH, after the sol being magnetically stirred for 30 min at room temperature, 1.92 g of Y dissolved in 20 mL of ethanol were added to the sol drop by drop keeping vigorous stirring for 30 min. Afterward, the mixed solution was added dropwise into another mixture consisting of 0.9 mL of deionized water and 10 mL of EtOH under roughly stirring to hydrolyze. DEA serves as a stabilizer to hinder the hydrolysis of TTBO. The chemical composition of the starting alkoxide solution was $\text{Y}:\text{TTBO}:\text{EtOH}:\text{H}_2\text{O}:\text{DEA} = 0.05:1:26.5:1:1$ in molar ratio. After continuously stirring for 2 h, a yellowish transparent sol of 5% Y doped TiO_2 in molar concentration was obtained, which was then aged for 24 h and served for film preparation.

Formation of YTF. YTF was prepared by a dip-coating method. Prior to the coating process, ITO glass substrates (sheet resistance $\leq 10 \, \Omega/\text{square}$) with dimension $50 \, \text{mm} \times 25 \, \text{mm} \times 1.5 \, \text{mm}$ were ultrasonically cleaned in potassium dichromate solutions and rinsed with anhydrous alcohol and deionized water. They were then dried at $100 \, ^\circ\text{C}$ in air. The film was obtained by dipping the substrate in the Y_2O_3 doped TiO_2 gel precursor solution bath and pulling upward with a constant speed of 4 cm/min using a TL0.01 dip-coater to keep uniform thickness of the film. After a layer was deposited, the glass was treated at $100 \, ^\circ\text{C}$ for 5 min and then coated with another layer. The thickness of the film was adjusted by dip-coating cycles. The films were coated with six layers and then were annealed at $500 \, ^\circ\text{C}$ for 2 h. To compare with the structure and property of YTF, the pure TiO_2 film (TF) was also synthesized through the same experimental process without doping of yttrium materials.

XRD and SEM Characterization. Crystal structures of TF and YTF were identified by X-ray diffraction (XRD) using a Rigaku D/max 2550 diffractometer with graphite monochromatized $\text{Cu K}\alpha$ radiation ($\lambda = 1.54056 \, \text{\AA}$). The different patterns were collected at a step of 0.02° in the 2θ range from 10° to 80° . The accelerating voltage and the applied current were 40 kV and 300 mA, respectively. Phases were measured using the Search/Match capabilities of the JADE 5.0 program along with the ICDD (International Center for Diffraction Data) powder diffraction file (PDF) database. The cross-sectional morphologies of the films were investigated by a scanning electron microscope (JSM-6490LV) at an operating accelerating voltage of 20 kV. Prior to SEM study, a thin layer of gold was deposited upon the sample surfaces.

XPS and AFM Characterization. The X-ray photoelectron spectroscopy (XPS) analysis was performed on a VG ESCALAB MK-II spectrometer equipped with an $\text{Mg K}\alpha$ (1253.6 eV) monochromator X-ray source with a power of 240 W. The test chamber pressure was maintained below 5×10^{-7} Torr during spectral acquisition. The XPS binding energy (BE) was internally referenced to the C 1s peak ($\text{BE} = 284.6 \, \text{eV}$). Survey spectra were obtained at a step of 0.4 eV, and high-resolution spectra were collected at a step of 0.05 eV. High-resolution spectra were resolved by fitting each peaks with Gaussian–Lorentz functions after subtracting the background using the ESCALAB V1.5 data processing software package under the constraint of setting a reasonable BE shift and characteristic full width at half-maximum range. Atomic concentrations were calculated by normalizing peak areas to the elemental sensitivity factor data provided by the ESCALAB database. The surface morphol-

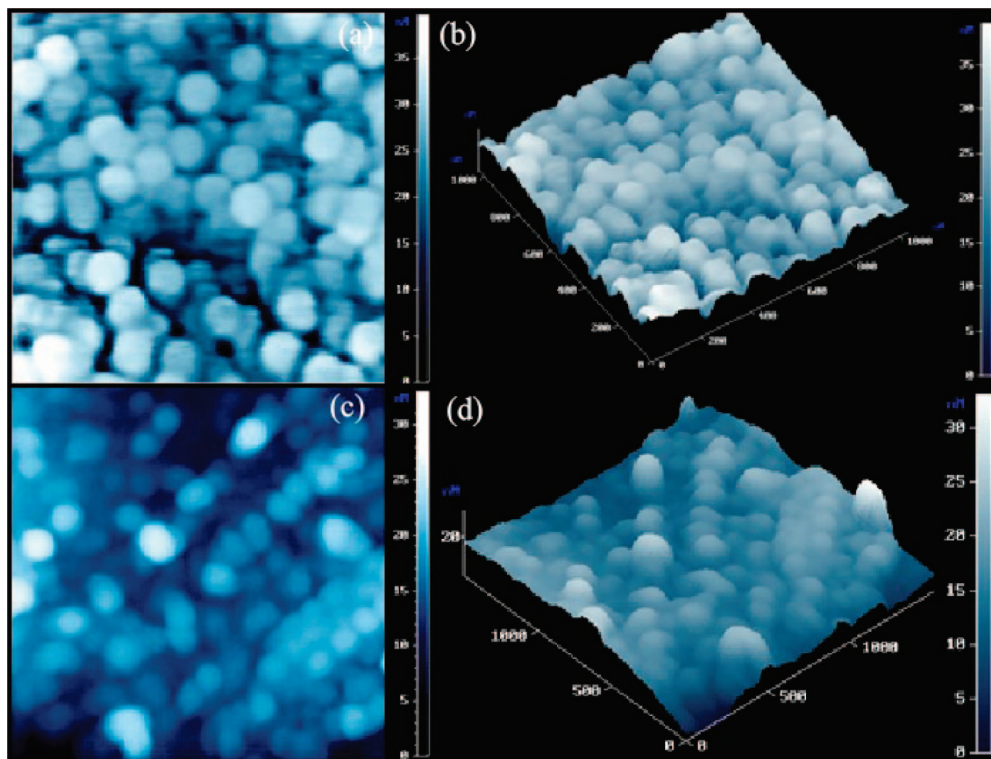


Figure 2. Two (a, c) and three (b, d) dimensional AFM images of TF (a, b) and YTF (c, d) films deposited on ITO substrate.

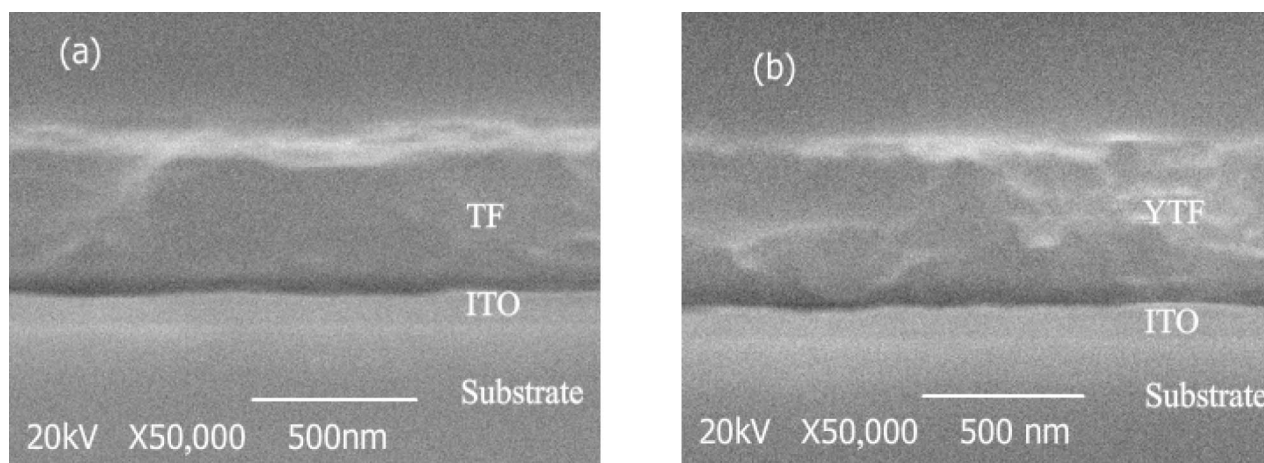


Figure 3. SEM cross-sectional morphologies of (a) TF and (b) YTF.

ogy was observed using a NT-MDT Solver P47 atomic force microscopy (AFM) with silicon probe tapping contact mode.

UV–Vis and Photoinduced Hydrophilicity Characterization. The ultraviolet–visible (UV–vis) absorption spectra of the samples were performed using a UV–visible spectrophotometer (UV-2450) with a wavelength range of 200–900 nm. Band gap energies of samples were estimated from absorption spectra. Hydrophilic properties were evaluated from the measurements of the water contact angles on the surface of the transparent TF and YTF with a commercial contact angle meter (JY-82) in an ambient environment. The sessile drop method was used for the contact angle measurements and the experimental error for the measurements is $\pm 1^\circ$. Deionized water was used as the water source in the contact angle measurement and the droplet volume used for the measurements is $1.5 \mu\text{L}$. Water droplets were placed at seven different positions for each sample and the average value was adopted as the water contact angle. The photoinduced hydrophilicity was evaluated by the in-time

variation of the water contact angle under daylight lamp (60 W) irradiation, the distance between the lamp and the sample was fixed at 15 cm.

Electrochemical Characterization. Electrochemical properties of TF and YTF were investigated in a three electrode cell using a CHI660a electrochemical workstation. The electrode was prepared on a film glass (area $1 \text{ cm} \times 1 \text{ cm}$) linked by copper lead and coated by epoxy resin except the working surface. This three-electrode cell was equipped with the prepared TF (or YTF) electrode as working electrode, platinum electrode as counter electrode and a standard calomel electrode (SCE) as reference electrode with $0.5 \text{ mol/L Na}_2\text{SO}_4$ solution as electrolyte. The impedance measurements were carried out with an amplitude of 5 mV over the open potential and added different potential at frequencies from 0.1 Hz to 10^5 Hz without light illumination. The data of photocurrent response were collected at open potential with and without irradiation. A 60 W daylight lamp was used as the light source.

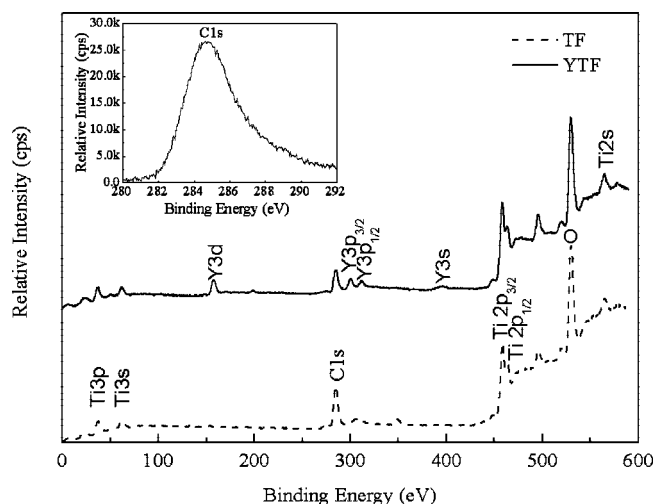


Figure 4. Full survey XPS spectra and C 1s survey curve of YTF (inserted profile).

Results and Discussion

Figure 1 shows the XRD patterns of TF and YTF deposited on ITO substrate. As shown in Figure 1, both materials have the same XRD pattern, no peaks due to other phases appear in the materials, indicating that the crystalline structure of TiO_2 film is not transformed irrespective of doping 5% Y_2O_3 . There is a broad hump in the low 2θ region $15\text{--}38^\circ$, which characterizes an amorphous phase corresponding to the glass substrate. It also can be seen that a sharp peak at $2\theta = 25.3^\circ$ superimposed on the broad hump, which clearly indicates the presence of a crystalline phase in addition to the amorphous phase. The peaks can be readily indexed to (101) diffraction peak of anatase phase TiO_2 (JCPDS 21-1272). It is worth noting that the diffraction peaks of YTF become wider than those of the TiO_2 film, indicating that the particle size of YTF is smaller than that of TF, which can be confirmed in the AFM images.

To demonstrate the surface morphologies of the films, two and three-dimensional AFM images of TF and YTF deposited on ITO glass substrate were shown in Figure 2. By AFM inspections, the films morphologies and particle size distributions were found to be similar at different parts of YTF. The nanoparticles of YTF exhibit spherical shape and the maximum protuberance (peak to peak) is 33.0 nm. The height and phase images for YTF are uniform, which indicates that the surfaces of the samples are smooth (the typical value of the root-mean-square roughness (rms) for a $1\text{ }\mu\text{m} \times 1\text{ }\mu\text{m}$ area is about 3.7 nm). In comparison, the rms and the maximum protuberance for TF are about 5.4 and 39.6 nm, respectively. The roughness of YTF is slightly smaller, which indicates that the surface of YTF is smoother than that of TF. The TF was composed of particles with mean size around 25.4 nm, and the particles of YTF became smaller, about 15.8 nm. This result indicates that doping of Y^{3+} ions could inhibit crystal growth of the TiO_2 film. The results agree with that of XRD. Figure 3 shows the film/substrate cross-sectional morphologies of TF and YTF, respectively; it can be seen that the thickness of YTF is about 480 nm and that of TF is about 450 nm. In addition, the thickness of conductive layer (ITO) about 120 nm, which is agreement with thickness parameter ($1200 \pm 80\text{ }\text{\AA}$) provided from the corporation.

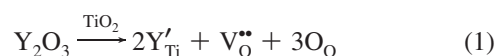
XPS measurements were performed to elucidate the surface chemical composition and the oxidation state for the as-synthesized samples. Figure 4 shows the XPS full survey spectra in the binding energy (BE) range of 0–600 eV for TF and YTF

deposited on ITO glass substrate. The inserted profile is the BE spectrum for C 1s electrons of YTF.

The XPS results indicated that four elements, namely, Ti, O, Y and C were present on the YTF surface, whereas the TF surface contained Ti, O and C elements. The trace amounts of carbon originate from the residual carbon in the film and the adventitious hydrocarbon in the XPS instrument itself. The chemical composition of YTF can be examined from the area of these elements XPS survey spectra. The measured Y, Ti and O atom concentrations are 6.2%, 38.7% and 55.1%, and the nominal atom concentrations are 3.1%, 31.8% and 65.1% in YTF, respectively. The determined concentration of Y was 2 times higher than that of the nominal one, suggesting that more Y species are present on the surface.

The high-resolution XPS regional spectra of the main constituents O 1s, Ti 2p and Y 3d were recorded for a more detailed analysis (Figure 5). The XPS spectra of O 1s in the figure were asymmetric; the right side was wider than the left from Figure 5a, indicating that several kinds of oxygen species were present at the surface, which can be fitted by Gaussian–Lorentz functions. As shown in Figure 5a, the O 1s band has been modified for YTF: a main peak emerged on the fitting line at BE of 529.6 eV that can be regarded as contributions from both the Ti–O and Y–O, which have similar binding energies, and two relatively low intensity peaks appeared at BE of 531.7 and 533.95 eV that may be attributed to the hydroxyl groups and the adsorbed H_2O on the surface of YTF.¹¹ On the other hand, the O 1s region of YT also can take into account three oxygen contributions; the peak at 529.76 eV was assigned to the oxygen bound to Ti and the others were the –OH and the adsorbed H_2O peaks. However, the peaks of the three oxygen contributions showed chemical shift and the intensity of the –OH peak was considerably increased by comparing TF with YTF. This clearly indicates that the YTF has more hydroxyl groups as well as surface-adsorbed water than that of TF, which would be beneficial to enhancing the hydrophilicity of YTF.

The BE of Ti $2p_{3/2}$ and O 1s of TF sample were 458.3 and 529.76 eV, respectively, which were consistent with the reported results of Pan.¹¹ The BE of O 1s and Ti 2p was decreased as indicated in Figure 5. As discussed by others,²⁵ a shift toward lower binding energy displays the successful incorporation of Y_2O_3 into the TiO_2 lattice. On the basis of solid state chemistry theory, the relatively higher concentration oxygen vacancies $\text{V}_\text{O}^\bullet$ can be created by doping Y_2O_3 to TiO_2 , the solid reaction equation can be written as follows:



It can be concluded that, in addition to more oxygen vacancies, the local chemical state has been significantly influenced by incorporation of Y_2O_3 into the TiO_2 lattice and the valence electron movement outside Ti atomic nucleus have been changed, which perhaps results in the shift of BE and the red shift of the absorption edge toward the visible-light region. With the incorporation of Y species, the intensity of O 1s considerably decreased and that of Ti 2p showed a few increase. This also suggests that relatively more Y and Ti species are present on the surface of the nanocomposite film. It can be concluded that the microstructure of YTF has changed and the active surface of YTF has been enhanced with the electronegative atom augment.

The survey spectrum for Y 3d region of nanocomposite film is shown in Figure 5c. The BE of Y $3d_{5/2}$ and Y $3d_{3/2}$ for YTF

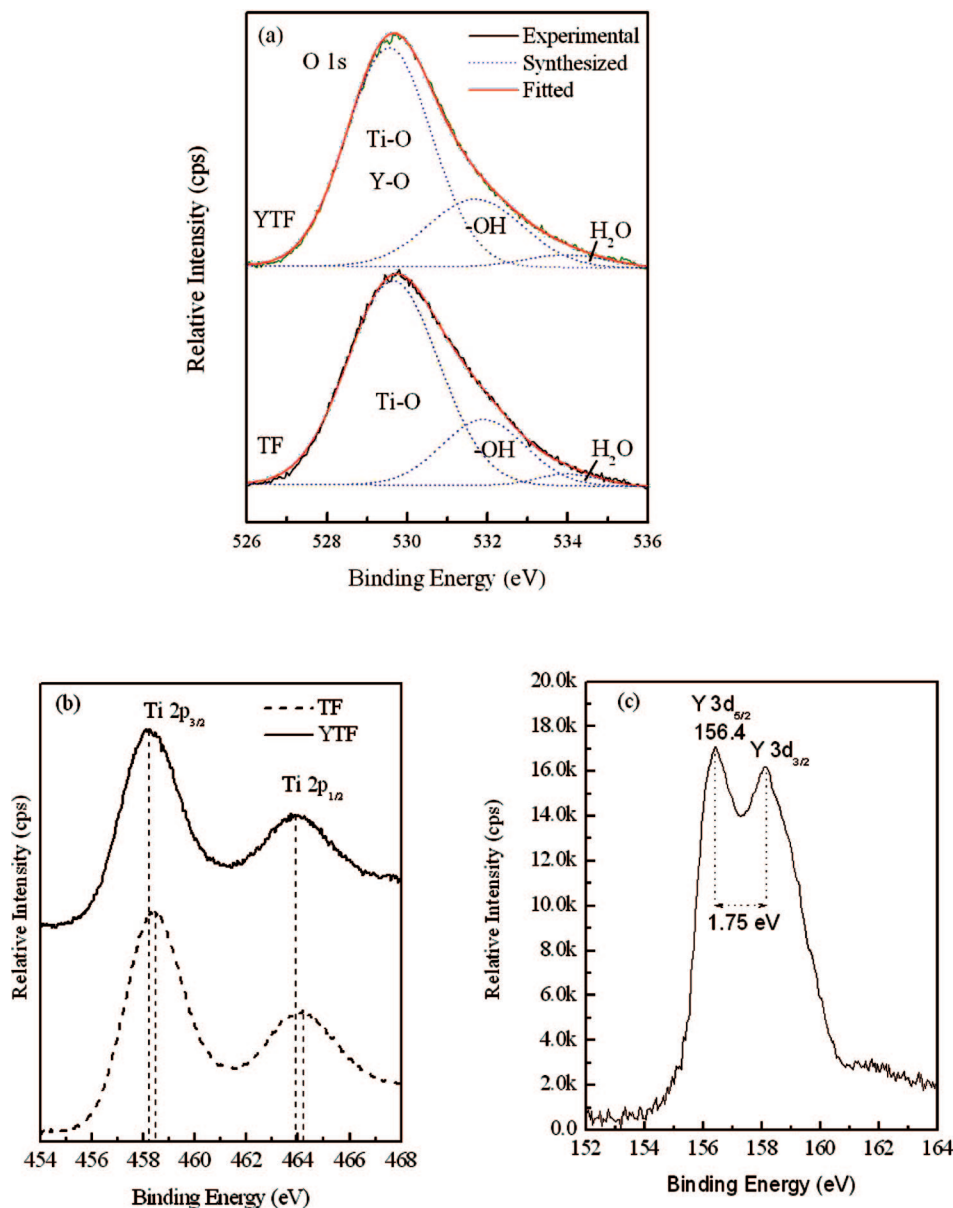


Figure 5. High-resolution XPS spectra and simulated Gaussian line shapes of (a) O 1s, (b) Ti 2p and (c) Y3d regions taken on the surface of TF and YTF.

is about 156.4 and 158.15 eV, respectively, with a spin-orbit splitting of 1.75 eV. The results are comparable with values of pure Y₂O₃ reported in the literature.²⁴ The center of the Y 3d_{5/2} peak corresponds to that of Y³⁺ oxidation state.

UV-vis spectroscopy was used to characterize the optical properties of the TiO₂ thin films. Figure 6a shows the absorption spectra of TF and YTF. There is a strong wide UV absorption band (320–400 nm) for the prepared TF and YTF. The UV-vis absorption spectra show that absorption edge for YTF has a red shift, which shifts toward visible light region, and the absorbance of YTF in visible light region is higher than that of TF. The enhanced visible light absorption may result from Y³⁺ replacing a portion of Ti⁴⁺ in TiO₂ crystalline, forming a new energy level at top of the valence band to generate a red shift. In addition, the absorption spectra in Figure 6a do not show the typical oscillations that appear when a high refractive index material is grown on a low refractive index substrate.²⁶ This is due to a combination of the following three factors: (a) The refractive index of the layers is very close to that of the substrate. (b) The films are very thin ($d < 100$ nm). (c) The films disperse

the light. Because the thickness of thin film is about 450–500 nm and the refractive index of ITO is lower than that of TiO₂, the third factor seems quite important here because absorption has a high value for all the range.

According to the data of the absorption spectra, the relation between the absorption coefficient (α) and incident photon energy ($h\nu$) can be estimated by using the equation^{27,28}

$$\alpha h\nu = A(h\nu - E_g)^2 \quad (2)$$

where α is the absorption coefficient, $h\nu = 1239.84/\lambda$ is the energy of excitation, λ is the wavelength, E_g is the band gap of the TiO₂ for indirect transition, and A is a constant that does not depend on photon energy.

A quantitative evaluation of the band gap energy (E_g) can be performed by plotting $(\alpha h\nu)^{1/2}$ versus $h\nu$ and extrapolated from linear part of the curve as shown in the Figure 6b. The intercept of the tangent to the plot will give a good approximation of the indirect band gap energies of the samples. The indirect band

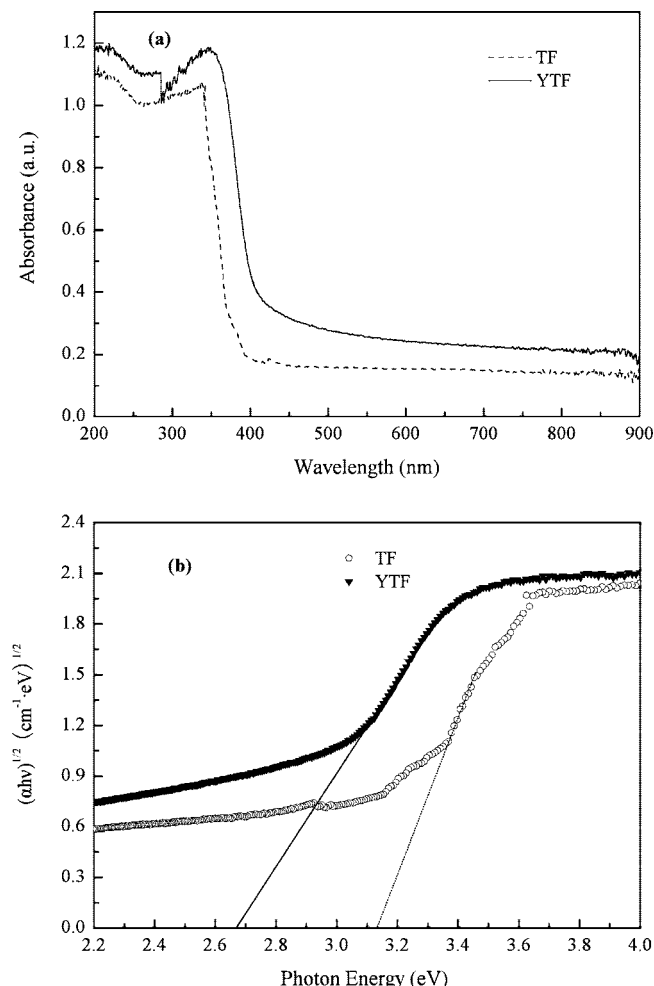


Figure 6. (a) UV-vis absorption spectra of TF and YTF deposited on ITO substrate and (b) plots of $(\alpha h\nu)^{1/2}$ versus $h\nu$ for indirect transition of TF and YTF.

gap energies estimated from the intercept of the tangents to the plots are 3.13 and 2.68 eV for TF and YTF, respectively. The optical band gap energy of TF was 3.13 eV, which was in agreement with the band gap energy (3.2 eV) of the anatase TiO_2 for indirect transition. From the results of the UV-vis spectra, the absorption edge of YTF shifts toward visible light region and the band gap energy of YTF decreases 0.45 eV than that of TF. The optical properties of YTF in visible light region are obviously improved after the incorporation of Y_2O_3 , which will probably make a good foundation for the investigation of TiO_2 films applied in photoelectrochemical and self-cleaning fields.

To investigate the surface wettability of TF and YTF, the contact angles of water droplets were measured both with and without daylight lamp irradiation under ambient conditions, the results are shown in Figure 7. From Figure 7, three trends can be easily observed: (a) The water contact angle of YTF has decreased 24° compared with that of TF. (b) All the water contact angles show noticeable decrease after daylight lamp irradiation. (c) After daylight lamp irradiation for 60 min, the water contact angle of YTF is only about 8° , which indicates superhydrophilicity. From Wenzel's equation ($\cos \theta^* = \gamma \cos \theta$, where γ is the film surface roughness, $\cos \theta$ is the classical contact angle depicted by Young equation, and θ^* is the measured real contact angle), the water contact angle for a rough but stoichiometric surface will be smaller than that for a smooth surface,²⁹ indicating that the hydrophilicity depends on the

surface property of the samples. As discussed above, the surface property of YTF has been changed by the incorporation of Y_2O_3 , and visible light can excite pairs of electrons and holes. Ti^{4+} sites are substituted by Y^{3+} ions, which gives one excess negative charge. The excess negative charge will trap the photoinduced electrons rapidly, making photogenerated holes possess more opportunities to combine with H_2O adsorbed on the film surface. The hydrophilicity is also believed to relate to the density of surface hydroxyl of the TiO_2 films. The surface hydroxyl can combine with water molecules to form hydrogen bond, resulting in good wettability. Photogenerated holes react with water to produce hydroxyl radicals, which are also beneficial to enhancing the hydrophilicity of YTF. So the visible light exciting photoinduced pairs of electrons and holes could be ascribed to the important contribution to the superhydrophilicity of YTF under daylight illumination. The obtained YTF is expected to have interesting applications in self-cleaning, antifogging and other potential areas.

Electrochemical impedance spectroscopy (EIS)^{30–33} is very effective for studying the mechanism and kinetics of complicated electrode reaction and offers an excellent method to test the equivalent circuit (EC) model used to describe the semiconductor/electrolyte interface. It is particularly desirable to be able, using impedance measurements, to represent the metal oxide/electrolyte interface in terms of passive electronic elements in the EC, the physical significance of which can be ascertained by variation of the electrode potential.

Figure 8 shows EIS analysis of TF and YTF electrodes at different added potential. As shown in Nyquist plots (Figure 8a), these spectra of YTF (TF) electrodes appeared two semicircles, which was also testified by two time constants in Bode plots (Figure 8b). The response at high frequency is related to the counter electrode/electrolyte interface, the charge-transfer resistance and double layer capacitance between working electrode/electrolyte interfaces are usually observed at low frequency.³³ On the basis of the assumable mechanism process, the EC represented, $R_s(C_1R_1)[Q_2(R_2O_2)]$, was used for fitting the impedance spectra obtained for both TF and YTF electrodes with ZSimDemo 3.20 software. Considering the EC in Figure 9, the elements with subscripts 1 and 2 are related to the contribution of the interfaces of counter electrode/electrolyte and working electrode/electrolyte, respectively. The ohmic serial resistance (R_s) corresponds to the electrolyte and the ITO resistance. C_1 and R_1 represent the charge-transfer resistance and capacitance, respectively, at the Pt counter electrode/electrolyte interface. R_2 and Q_2 represent the charge-transfer resistance and double charge layer capacitance, respectively, at the YTF (TF) working electrode/electrolyte interface. Q is the symbol for the constant phase element, CPE (its parameters are Y_{O1} and n). The CPE is the consequence of the nonideal frequency dependent capacitance of the working electrode/electrolyte interface and has been extensively discussed.^{32,33} O_2 depends on the parameters Y_{O2} and B , accounts for a finite-length Warburg diffusion (Z_D).

The CPE is a nonideal frequency dependent capacitance, a characteristic that can be associated with a distribution of relaxation times or with a nonuniform distribution of current due to material heterogeneity.³³ Its admittance is expressed by eq 3, where n is a constant ranging from $0 \leq n \leq 1$.

$$Y = Y_{O1}(j\omega)^n \quad (3)$$

The impedance of the Warburg diffusion in a finite-length region of length l_e (which might be the thickness between the

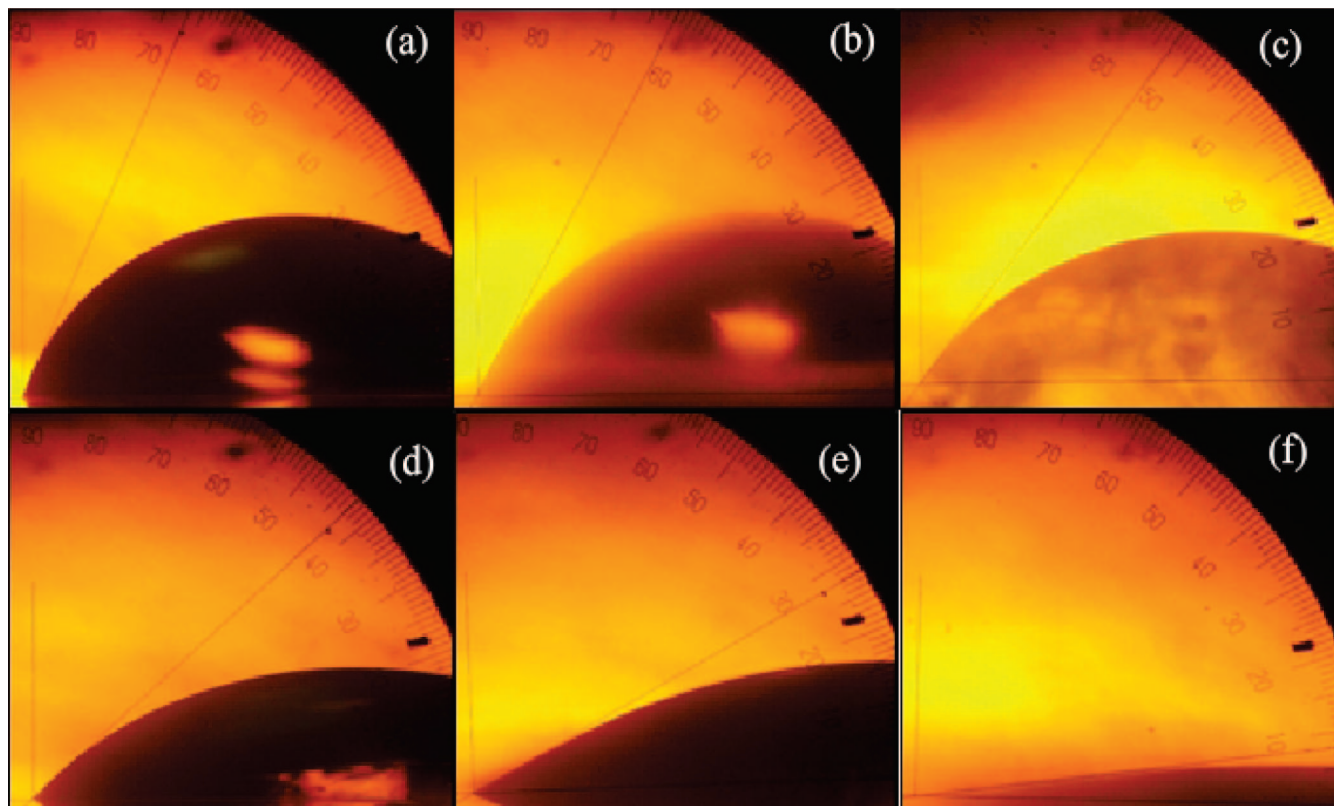


Figure 7. Contact angles of water droplets picture collected on the surface of TF (a) without daylight lamp irradiation, with daylight lamp irradiation (b) 20 min, (c) 60 min, and YTF (d) without daylight lamp irradiation, with daylight lamp irradiation (e) 20 min, (f) 60 min, respectively.

electrodes) can be expressed by the following equation (4), where $R_{\text{Dif}} = B/Y_{\text{O}_2}$, $\tau = B^2 = l_0/D$ and D is the diffusion coefficient of the diffusing species.³³

$$Z_{\text{Dif}} = R_{\text{Dif}} \{ [\tanh(j\omega\tau)]^{1/2} / (j\omega\tau)^{1/2} \} \quad (4)$$

The experimental data are represented by symbols, and solid lines correspond to the fitted data obtained using the EC. In the low-frequency range, the arc increased in size with increasing voltage, indicating the decrease in the space charge layer capacitance. The fitted data are coherent with the experimental data within an error of 5%. It can be concluded that the EC provided a reliable description for the electrochemical systems. The basic data obtained by fitting the experimental spectra with the EC at different potentials in frequency from 10^{-1} to 10^5 Hz are listed in Table 1.

The space charge layer capacitance (C_{sc}) can be related to the donor concentration (N_{D}) and the flat-band potential (V_{fb}) of the semiconductor using the Mott–Schottky equation:^{34,35}

$$C_{\text{sc}}^{-2} = \frac{2}{q\epsilon\epsilon_0 N_{\text{D}} A^2} \left(V - V_{\text{fb}} - \frac{\kappa T}{q} \right) \quad (5)$$

where q is the elementary charge, ϵ_0 is vacuum dielectric constants, ϵ is the relative dielectric constant, taken approximately as 55 for anatase TiO₂ film,³⁵ A is film electrode area, V is the electrode potential, k is the Boltzmann constant and T is the absolute temperature. The linearity of the relation C_{sc}^{-2} vs V implies that the main voltage drop occurs over the space charge layer. Figure 10 presents typical Mott–Schottky

plots of C_{sc}^{-2} vs V for TF and YTF electrodes in the high frequency ranging from 0.1 Hz to 10^5 kHz.

The positive slope of the Mott–Schottky straight line indicates that the samples are the typical n-type semiconductor. The slope (Z) and the intercept (V_0) at $C_{\text{sc}}^{-2} = 0$ correspond to a critical potential of the Mott–Schottky curves, the V_{fb} and N_{D} are expressed by following equations:

$$V_{\text{fb}} = V_0 - \frac{kT}{q} \quad (6)$$

$$N_{\text{D}} = \frac{2}{q\epsilon\epsilon_0 Z A^2} \quad (7)$$

The V_{fb} values for TF and YTF electrodes are -0.12 and -0.71 V, respectively. The estimated value of the donor concentration N_{D} for YTF is $1.05 \times 10^{20} \text{ cm}^{-3}$, which enhances 1 order of magnitude as N_{D} ($1.57 \times 10^{19} \text{ cm}^{-3}$) obtained for TF. TF presents lower donor concentration than YTF, indicating that less charge transfer occurred and it impedes the charge transfer more effectively than the latter. The thickness of the space charge layer can be estimated from the following equation:^{35,36}

$$d_{\text{sc}} = \left(\frac{2\epsilon\epsilon_0 |V - V_{\text{fb}}|}{qN_{\text{D}}} \right)^{1/2} \quad (8)$$

The estimated thicknesses of the space charge layer at potential of 0.4 V for TF and YTF are 134.2 and 96.8 nm, respectively.

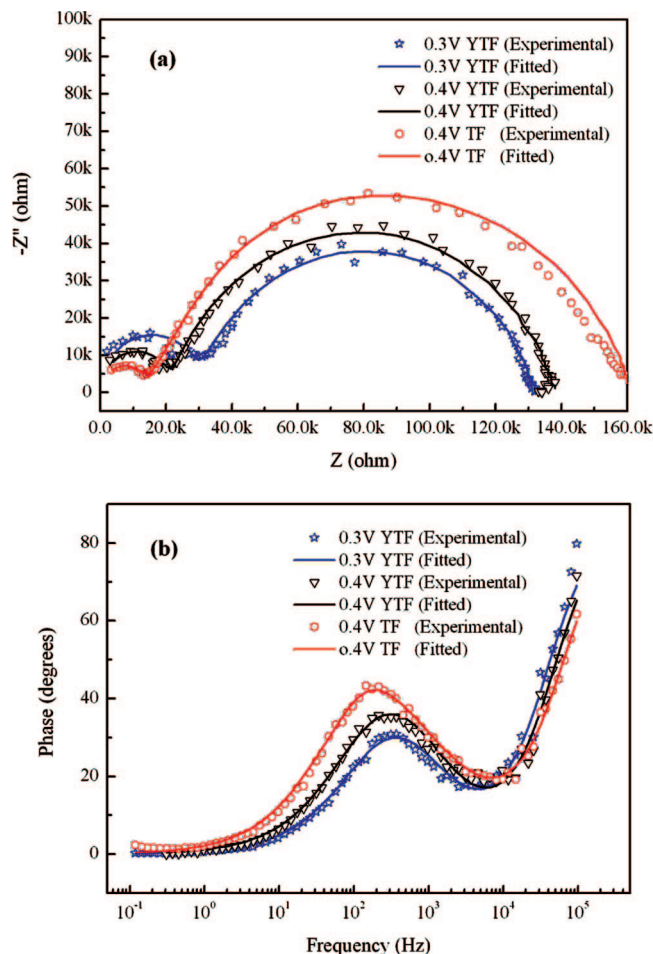


Figure 8. Nyquist (a) and Bode (b) diagrams of the impedance spectra at frequencies from 10^{-1} to 10^5 Hz obtained without light illumination for TF and YTF electrodes in 0.5 mol/L Na_2SO_4 electrolyte. Experimental data are represented by symbols and solid lines correspond to fits obtained with ZSimDemo 3.20 software using the EC in Figure 9. Added potential: (\star) 0.3 V for YTF, (∇) 0.4 V for YTF and (\circ) 0.4 V for TF.

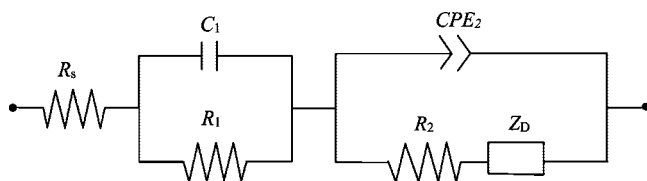


Figure 9. Equivalent circuit (EC), describing the interface in the three electrode system composed of ITO (substrate)/YTF (or TF)/electrolyte/Pt, used as the curve fitting of the impedance spectra for TF and YTF electrodes: R_s , electrolyte and ITO resistance; R_1 and C_1 , charge-transfer resistance and capacitance at the interface of Pt counter electrode/electrolyte; R_2 , CPE_2 and Z_D , charge-transfer resistance, constant phase element and finite-length Warburg diffusion impedance at interface of YTF (TF) working electrode/electrolyte.

Figure 11 shows that when anodic bias potential is present, an obvious anodic current is obtained, and introduction of the Y_2O_3 contributes a lot to the current in external current. The photocurrent can be enhanced by the illumination with a daylight lamp due to the photogenerated electrons. The current increases with increasing anodic bias, which is expected from the behavior of an n-type semiconductor, and the result is coherent with results found by Mott–Schottky curves. Another interesting behavior of the I – V characteristics is the observation of a zero-current at potential -0.41 and -0.82 V for TF and YTF, whereas the zero-current becomes -0.65 and -1.11 V, respec-

TABLE 1: Parameters Obtained by Fitting the Impedance Spectra of YTF (TF) at Potential from 0 to 0.4 V Electrode Using the EC $R_s(C_1R_1)[Q_2(R_2O_2)]$ in Figure 9

potential/V	R_s/Ω	C_1/nF	$R_1/\text{k}\Omega$	Q_2		n	O_2		
				$Y_{O1}/\mu\text{F s}^{n-1}$			$R_2/\text{k}\Omega$	Y_{O2}/S	$B/\text{s}^{1/2}$
0.4 (YTF)	24.8	18.7	40.5	7.29	0.782	31.2	0.031	3.7	
0.3 (YTF)	25.4	19.3	39.9	7.66	0.792	31.8	0.033	3.9	
0.2 (YTF)	25.9	19.6	45.2	8.04	0.804	32.1	0.035	3.8	
0.1 (YTF)	26.6	20.3	48.1	8.42	0.824	33.4	0.034	4.0	
0 (YTF)	27.4	21.5	49.7	9.29	0.841	34.3	0.038	4.2	
0.4 (TF)	26.2	3.8	31.7	2.92	0.769	19.1	0.008	1.4	
0.3 (TF)	26.3	3.6	31.2	3.35	0.780	16.9	0.012	1.2	
0.2 (TF)	26.1	4.1	28.6	3.87	0.761	17.6	0.017	1.3	
0.1 (TF)	26.4	4.8	33.2	4.91	0.770	18.6	0.021	1.3	
0 (TF)	26.8	5.6	39.8	6.26	0.686	23.8	0.023	1.6	

tively, after illumination with a daylight lamp. This potential, which is close to the flat-band potential of the metal oxide semiconductor, indicates that all the generated charge carriers are lost in the recombination process at this potential. With the doping of Y_2O_3 and illumination with a daylight lamp, this zero-current potential shift to negative potential indicates that YTF produces anodic current more easily. The positive current was

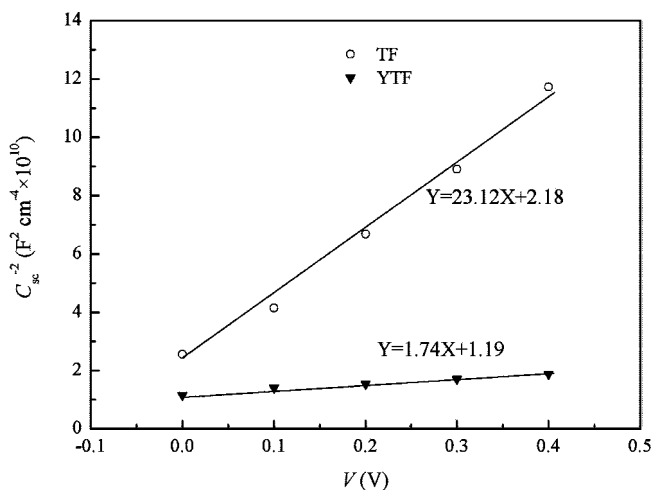


Figure 10. Mott–Schottky plots of C_{sc}^{-2} vs V for TF and YTF electrode in the high-frequency range from 0.1 Hz to 10^5 kHz.

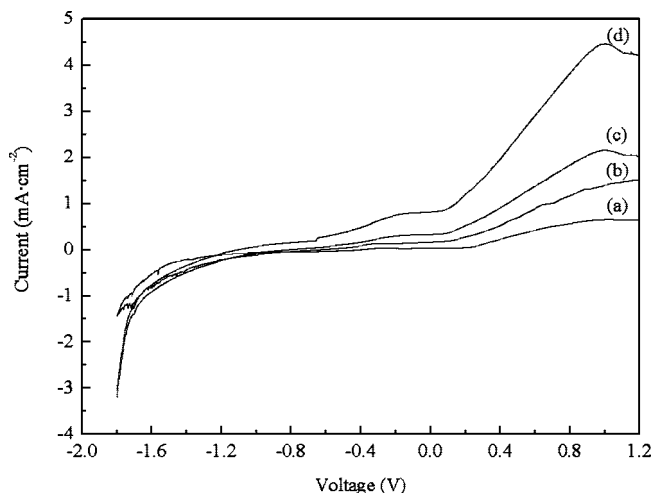


Figure 11. I – V characteristic curves of TF (a) without daylight lamp irradiation, (b) with daylight lamp irradiation for 30 min and YTF, (c) without daylight lamp irradiation, and (d) with daylight lamp irradiation for 30 min, respectively (reference electrode, SCE; scanning rate, $10 \text{ mV} \cdot \text{s}^{-1}$; and electrolyte, 0.5 mol/L Na_2SO_4).

observed in the range -0.3 to 0 V under no daylight lamp irradiation. This phenomenon could probably be explained in terms of the relatively higher concentration oxygen vacancies $V_{\text{O}}^{\bullet\bullet}$ created by doping Y₂O₃ to TiO₂. The open potential was about -0.8 V for YTF without daylight lamp irradiation, indicating that the positive bias potential was added to the working electrode in the range -0.3 to 0 V. The positive current appeared due to transferring the oxygen vacancies under the positive bias potential. On the other hand, the impedance arc for the YTF electrode decreased in size than that of TF in the low-frequency range, indicating the decrease in the corresponding capacitance constant and the decrease in impedance arising from the Faraday current. Therefore, the electrode reaction took place more easily and the energy barrier became smaller, the electrode reaction rate accelerated.

Conclusions

In summary, the 5% Y₂O₃ doped TiO₂ nanocomposite film (YTF) deposited on ITO glass substrate has been synthesized by the sol-gel dip-coating method. The crystalline structure, surface morphology, surface chemical composition of TF and YTF were characterized by using different methods. The optical, electrochemical and photoinduced hydrophilic properties of YTF are primarily investigated and compared with that of TF.

The results demonstrate that YTF with spherical shape particles of 15.8 nm was smoother. The binding energy appears chemical shift and relatively more Y and Ti species are present on the surface, indicating that active surfaces of the nanocomposite film have been enhanced with the electronegative atom augment. The optical properties of YTF in visible light region have been obviously improved because the absorption edge has a red shift and the optical properties of YTF in visible light region have been obviously improved. YTF appears super hydrophilicity after daylight lamp irradiation. From the results of electrochemical impedance spectroscopy, the $R_s(C_1R_1)[Q_2(R_2O_2)]$ equivalent circuit model provided a reliable description for the electrochemical systems. Based on the Mott-Schottky equation, the donor concentration (N_D) for YTF is $1.05 \times 10^{20} \text{ cm}^{-3}$, which enhances 1 order of magnitude than that for TF, the flat-band potential (V_{fb}) and the space charge layer (d_{sc}) are obvious decrease. These results disclose intriguing perspectives for the development of self-cleaning and photo-electrochemistry. The importance of this study also lies in the fact that it reveals the possibility of expanding the related work from YTF to other oxide semiconductors for developing new functional nanomaterials.

Acknowledgment. This work was supported by the National Natural Science Foundation of China (50774095), the Program for the New Century Excellent Talents in University (NCET-05-0695), the Excellent Youth Foundation of Central South University and the Postgraduate Educational Innovation Engineering of Central South University (1343-76236).

References and Notes

- (1) Fujishima, A.; Honda, A. *Nature* **1972**, 238, 37.
- (2) Doh, J. G.; Hong, J. S.; Vittal, R.; Kang, M. G.; Park, N. G.; Kim, K. J. *Chem. Mater.* **2004**, 16, 493.
- (3) Zhang, D.; Yoshida, T.; Oekermann, T.; Furuta, K.; Minoura, H. *Adv. Funct. Mater.* **2006**, 16, 1228.
- (4) Rothschild, A.; Edelman, F.; Komem, Y.; Cosandey, F. *Sens. Actuators B-Chem.* **2000**, 67, 282.
- (5) Shankar, K.; Tep, K. C.; Mor, G. K.; Grimes, C. A. *J. Phys. D: Appl. Phys.* **2006**, 39, 2361.
- (6) Diebold, U. *Appl. Phys. A: Mater. Sci. Process.* **2003**, 76, 681.
- (7) Choi, S. Y.; Mamak, M.; Speakman, S.; Chopra, N.; Ozin, G. A. *Small* **2005**, 1 (2), 226.
- (8) Chu, S. Z.; Inoue, S.; Wada, K.; Li, D.; Suzuki, J. *Langmuir* **2005**, 21, 8035.
- (9) Kim, K. D.; Han, D. N.; Lee, J. B.; Kim, H. T. *Scr. Mater.* **2006**, 54, 143.
- (10) Wang, H.; Lewis, J. P. *J. Phys.: Condens. Matter* **2005**, 17, 209.
- (11) Pan, J. H.; Lee, W. I. *Chem. Mater.* **2006**, 18, 847.
- (12) Bavykin, D. V.; Friedrich, J. M.; Walsh, F. C. *Adv. Mater.* **2006**, 18, 2807.
- (13) Vinodgopal, K.; Bedja, I.; Kamat, P. V. *Chem. Mater.* **1996**, 8, 2180.
- (14) Tacconi, N. R.; Mrkic, M.; Rajeshwar, K. *Langmuir* **2000**, 16, 8426.
- (15) Poznyak, S. K.; Talapin, D. V.; Kulak, A. I. *J. Phys. Chem. B* **2001**, 105, 4816.
- (16) Kwon, C. H.; Kim, J. H.; Jung, I. S.; Shin, H.; Yoon, K. H. *Ceram. Int.* **2003**, 29, 851.
- (17) Bartl, M. H.; Puls, S. P.; Tang, J.; Lichtenegger, H. C.; Stucky, G. D. *Angew. Chem., Int. Ed.* **2004**, 43, 3037.
- (18) Liang, L. P.; Sheng, Y. G.; Xu, Y.; Wu, D.; Sun, Y. H. *Thin Solid Films* **2007**, 515, 7765.
- (19) Barreca, D.; Comini, E.; Ferrucci, A. P.; Gasparotto, A.; Maccato, C.; Maragno, C.; Sberveglieri, G.; Tondello, E. *Chem. Mater.* **2007**, 19, 5642.
- (20) Chen, D.; Zhang, H.; Hu, S.; Li, J. H. *J. Phys. Chem. C* **2008**, 112, 117.
- (21) Randeniya, L. K.; Bendavid, A.; Martin, P. J.; Preston, E. W. *J. Phys. Chem. C* **2007**, 111, 18334.
- (22) Yolanda, C.; Beatriz, J. L.; Cedric, B.; Bruno, V.; David, G.; Clement, S. *Microporous Mesoporous Mater.* **2007**, 103, 273.
- (23) Ranade, M. R.; Elder, S. H.; Navrotsky, A. *Chem. Mater.* **2002**, 14, 1107.
- (24) Sun, G. B.; Hidajat, K.; Wu, X. S.; Kawi, S. *Appl. Catal. B: Environ.* **2008**, 81, 303.
- (25) Du, X. Y.; Wang, Y.; Mu, Y. Y.; Gui, L. L.; Wang, P.; Tang, Y. Q. *Chem. Mater.* **2002**, 14, 3953.
- (26) Swanepoel, R. *J. Phys. E: Sci. Instrum.* **1983**, 16, 1214.
- (27) Hagfeldt, A.; Gratzel, M. *Chem. Rev.* **1995**, 95, 49.
- (28) Gracia, F.; Holgado, J. P.; Caballero, A.; Gonzalez, A. R. *J. Phys. Chem. B* **2004**, 108, 17466.
- (29) Iketani, K.; Sun, R. D.; Toki, M.; Hirota, K.; Yamaguchi, O. *Mater. Sci. Eng. B* **2004**, 108, 187.
- (30) Adachi, M.; Sakamoto, M.; Jiu, J. T.; Ogata, Y.; Isoda, S. *J. Phys. Chem. B* **2006**, 110, 13872.
- (31) Leng, W. H.; Zhang, Z.; Zhang, J. Q.; Cao, C. N. *J. Phys. Chem. B* **2005**, 109, 15008.
- (32) Liu, H.; Cheng, S. A.; Wu, M.; Wu, H. J.; Zhang, J. Q.; Li, W. Z.; Cao, C. N. *J. Phys. Chem. A* **2000**, 104, 7016.
- (33) Longo, C.; Nogueira, A. F.; Paoli, M. A. *J. Phys. Chem. B* **2002**, 106, 5925.
- (34) Randeniya, L. K.; Bendavid, A.; Martin, P. J.; Preston, E. W. *J. Phys. Chem. C* **2007**, 111, 18334.
- (35) Krol, R. V.; Goossens, A.; Schoonman, J. *J. Electrochem. Soc.* **1997**, 144 (5), 1723.
- (36) Hukovic, M. M.; Grubac, Z. *J. Phys. Chem. B* **1998**, 102, 7406.